LETTER

doi:10.1038/nature18594

An early geodynamo driven by exsolution of mantle components from Earth's core

James Badro[1,2], Julien Siebert[1] & Francis Nimmo[3]

Recent palaeomagnetic observations[1] report the existence of a magnetic field on Earth that is at least 3.45 billion years old. Compositional buoyancy caused by inner-core growth[2] is the primary driver of Earth's present-day geodynamo[3–5], but the inner core is too young[6] to explain the existence of a magnetic field before about one billion years ago. Theoretical models[7] propose that the exsolution of magnesium oxide—the major constituent of Earth's mantle—from the core provided a major source of the energy required to drive an early dynamo, but experimental evidence for the incorporation of mantle components into the core has been lacking. Indeed, terrestrial core formation occurred in the early molten Earth by gravitational segregation of immiscible metal and silicate melts, transporting iron-loving (siderophile) elements from the silicate mantle to the metallic core[8–10] and leaving rock-loving (lithophile) mantle components behind. Here we present experiments showing that magnesium oxide dissolves in core-forming iron melt at very high temperatures. Using core-formation models[11], we show that extreme events during Earth's accretion (such as the Moon-forming giant impact[12]) could have contributed large amounts of magnesium to the early core. As the core subsequently cooled, exsolution[7] of buoyant magnesium oxide would have taken place at the core–mantle boundary, generating a substantial amount of gravitational energy as a result of compositional buoyancy. This amount of energy is comparable to, if not more than, that produced by inner-core growth, resolving the conundrum posed by the existence of an ancient magnetic field prior to the formation of the inner core.

At the present day, the geodynamo is powered primarily by compositional buoyancy[3–5] due to the crystallization of the inner core from the outer core, which started around one billion years ago[2,6]. This creates a conundrum as to the origin of the early field; the inner core is certainly much younger than 3.45 Gyr, so a process other than its crystallization must have driven the early field.

Whether an early dynamo could have been driven by thermal buoyancy alone depends on the power extracted from the core by the mantle, which is uncertain[13]. It has been suggested[7,14–16] that light elements dissolved in the core during core formation could have exsolved early in Earth's history as the core cooled; the resulting compositional buoyancy would have generated enough energy to fuel an early geodynamo. Magnesium exsolution before inner-core growth has been proposed[7,15] as a mechanism paralleling oxygen and/or silicon exsolution after inner-core crystallization. The prerequisite however is that magnesium must dissolve in iron during core formation.

To assess the plausibility of that mechanism, we experimentally investigated the solubility of magnesium in molten iron in equilibrium with basaltic and pyrolitic silicate melts at extremely high temperature. The experiments were performed in a laser-heated diamond-anvil cell, in which thin disks of pure iron were sandwiched between two pyrolite or tholeiite glass disks of identical composition, thickness and diameter. The assembly was compressed to 35–74 GPa and laser-heated between 3,300 K and 4,400 K for 30–60 s. After quench and decompression, thin sections were removed from the centre of the laser-heated spot using a crossbeam focused-ion-beam microscope. The thin sections were imaged by high-resolution field-emission scanning electron microscopy and all showed a coalesced spherical iron ball surrounded by molten silicate (Extended Data Fig. 1), confirming that the sample (metal and silicate) was fully molten during equilibration. The composition of the metal and silicate was analysed using high-resolution electron probe microanalysis (see Methods).

Magnesium solubility in iron takes place according to

$$\mathrm{MgO}^{\mathrm{silicate}} \rightleftharpoons \mathrm{Mg}^{\mathrm{metal}} + \mathrm{O}^{\mathrm{metal}} \qquad (1)$$

with an equilibrium constant K_{Mg} of $\log(K_{\mathrm{Mg}}) = a + b/T + cP/T$, where T is temperature in kelvin and P is pressure in gigapascals. The parameters (a, b and c; see Methods) were determined from a least-squares fit to our data to obtain

$$\log(K_{\mathrm{Mg}}) = 1.23(0.7) - \frac{18,816(2,600)}{T} \qquad (2)$$

where the numbers in parentheses are the standard errors of the parameters. Parameter c was found to be statistically irrelevant (the error on the parameter is larger that the parameter itself and so it does not pass the F test), which indicates that MgO solubility is independent of pressure. The regression is plotted along with the experimental data in Fig. 1 and shows a fit with $R^2 = 0.96$. This confirms that the reaction shown in equation (1) accurately describes the process of MgO dissolution in iron and that pressure has no observable effect. Aluminium dissolution also takes place and can similarly be quantified (Extended Data Fig. 2), as discussed in Methods. However, at extreme temperatures the two-component system reduces to a single homogeneous miscible (solvus) metal-silicate phase[17]. In that case, the reaction shown equation (1) ceases to describe the system because neither of the phases (metal nor silicate) is present. The MgO content of the homogeneous melt is then solely a function of the original bulk composition of the two-phase system.

To estimate the amount of MgO that can be dissolved in the core during formation, we ran a series of multistage core-formation models[11], whereby the planet was grown to its present mass by iterative accretion and core–mantle differentiation of material (see Methods). The magnesium concentrations in the growing core and mantle were calculated iteratively along with other lithophile (O, Si and Al) and siderophile (Ni, Co, Cr and V) elements. More than 8,000 simulations were performed to sample the parameter space fully, and only geochemically consistent models (for which the final concentrations of Ni, Co, Cr and V in the silicate match present-day mantle abundances) were retained[11].

For core formation without a giant impact, we found a maximum of 0.8 wt% MgO in the core, in the most favourable (hottest geotherm and deepest magma ocean) case. For a present-day temperature[18] at the core–mantle boundary (CMB) of 4,100 K, the MgO equilibrium

---

[1]Institut de Physique du Globe de Paris, Université Sorbonne Paris Cité, 75005 Paris, France. [2]Earth and Planetary Science Laboratory, École Polytechnique Fédérale de Lausanne, CH-1015, Lausanne, Switzerland. [3]Department of Earth and Planetary Sciences, University of California Santa Cruz, Santa Cruz, California 95064, USA.

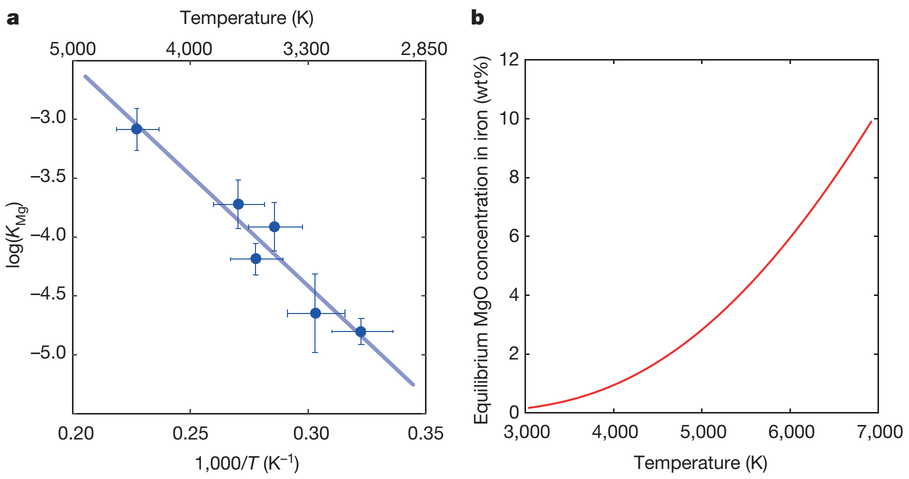

Figure 1 | Magnesium solubility in metallic iron melt at high pressure and temperature. **a**, Equilibrium constant for MgO dissolution in iron ($K_{\rm Mg}$) as a function of reciprocal temperature (1,000/T) (equation (2)). The experimental data are from Extended Data Table 1. The line corresponds to the least-squares linear fit to the data, and the error bars correspond to 1σ uncertainties. A comparison with extrapolation from density functional theory (DFT) calculations[17] is shown in Extended Data Fig. 2. **b**, The resulting MgO concentration in iron in equilibrium with pyrolite as a function of temperature. This is obtained by rewriting equation (2) to obtain $X_{\rm Mg}^{\rm metal} = 2.91\exp(-21,662/T)$, where T is temperature in kelvin, and then converting Mg molar fractions to MgO weight fractions. For an extended version of this graph, see Extended Data Fig. 6.

value (saturation threshold) in the core is 1.1 wt% (Fig. 1b). The core is therefore under-saturated in MgO so that any primordial magnesium dissolved during formation would not exsolve to the mantle.

We then ran a series of core-formation models that involve a final giant impact. In the Moon-forming giant-impact scenario[12], the impactor is typically thought of as a Mars-sized planetary embryo, but the masses used in models range from 2.5% to 20% of Earth's mass[19,20]. With such a size, the impactor is a differentiated object with a core and mantle, and the temperatures during the impact are sufficiently high that the impactor core and the surrounding silicate mantle turn into a single miscible metal-silicate phase (see Methods). As this dense silicate-saturated metallic object (hereafter called the 'hybridized impactor core', HIC) merges with Earth's core, it strongly increases the lithophile-element content of Earth's core. We calculated the composition of the HIC as a function of impactor size (Fig. 2a) by assessing its dilution ratio[21] (see Methods) in the magma ocean, that is, the relative mass of magma ocean with which the impactor core interacts. The amounts of Mg, Si and O brought by the HIC to Earth's core are plotted in Fig. 2b.

The total MgO dissolved in the core (Extended Data Fig. 3) ranges between 1.6 wt% and 3.6 wt%. Those values are higher than the saturation value of 1.1 wt% at the present-day CMB, which implies that the core became over-saturated in MgO as it cooled. The excess MgO must have exsolved to the mantle and provided a large source of potential energy[7] to drive an early dynamo. Because MgO solubility depends on temperature, but not on pressure, MgO exsolution in the core takes place at the CMB, where the temperature is lowest. As MgO exsolves from the metal, the residue becomes denser and sinks, and is replaced by lighter MgO-bearing metal. This process ensures that the entire core is processed at the CMB, so that the equilibrium concentration at the CMB (Fig. 1b) sets the concentration in the whole core. We estimated the energy released by MgO exsolution by calculating the difference in gravitational energies ($\Delta E_{\rm grav}$) of the core before and after exsolution, with the gravitational energy in each state given by

$$E_{\rm grav} = -\int_0^R \frac{GM(r)}{r} 4\pi r^2 \rho(r) {\rm d}r \qquad (3)$$

in which G is the gravitational constant, $M(r)$ is the mass of the core within a radius r, $\rho(r)$ is the density of the core at radius r and R is the radius of the core.

The energy release depends on how the HIC mixes with Earth's core, as shown by the dependence on $\rho(r)$ in equation (3). We investigated two extreme models of mixing: (i) full mixing of the HIC with Earth's core producing a homogeneous core and (ii) full layering whereby the HIC sits atop Earth's core (see Methods). The energy release as a function of impactor size is plotted in Fig. 3. In the mixed case, the energy release yields $(1–5.5) \times 10^{29}$ J. For comparison, the total energy release from inner-core growth (latent heat and buoyancy) is[2,6] $(0.9–1.7) \times 10^{29}$ J. The layered model provides less energy for small impacts (Fig. 3), but again reaches and exceeds the energy released by inner-core growth for Mars-sized or larger impactors.

Because MgO solubility depends only on temperature, the power release and onset time of MgO exsolution depend on the temperature evolution at the CMB, which itself depends on the initial MgO concentration in the core (see Methods). Although the early evolution of CMB temperature is uncertain, as an example we adopt an *a priori* CMB temperature[18] model. Prior to inner-core growth, the exsolution rate is high, as shown in Extended Data Fig. 4, and generates power in excess of about 3 TW (a conservative estimate of the amount of power

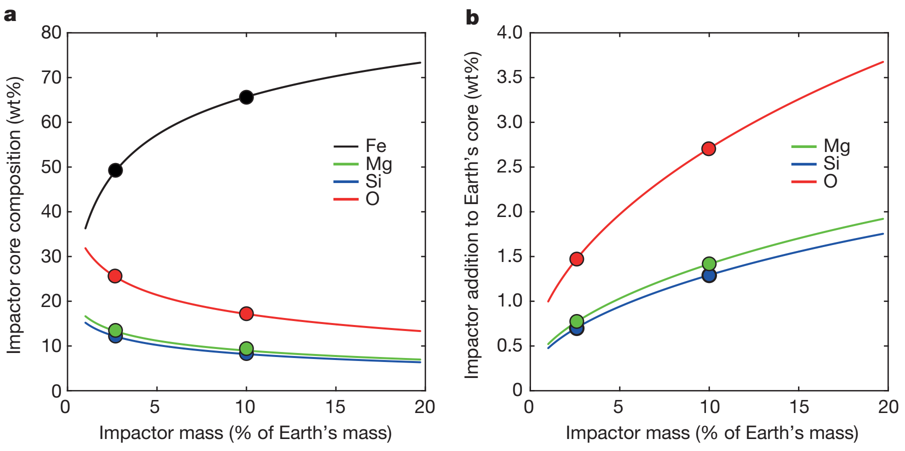

Figure 2 | Composition of the core of the giant impactor after equilibration in the magma ocean, and its effect on Earth's core composition. **a**, The composition of the hybridized impactor core (HIC) plotted as a function of impactor mass. Smaller impactors interact and equilibrate with larger relative amounts of magma ocean material; they 'swell' (see Extended Data Fig. 7) and become very enriched in Mg, Si and O. **b**, The compositional imprint of the giant impact on the core; between 2% and 8% of the total mass of the core consists of mantle material transported by the HIC. The Si and O concentrations added to the core are lower than the amounts present in the core before the impact[23]. This shows that the major contribution of the giant impact to core chemistry is the magnesium influx. The Mars-size impact[19] (10% of Earth's mass) and 'fast-spinning' impact[20] (2.5% of Earth's mass) are highlighted by circles in both panels.

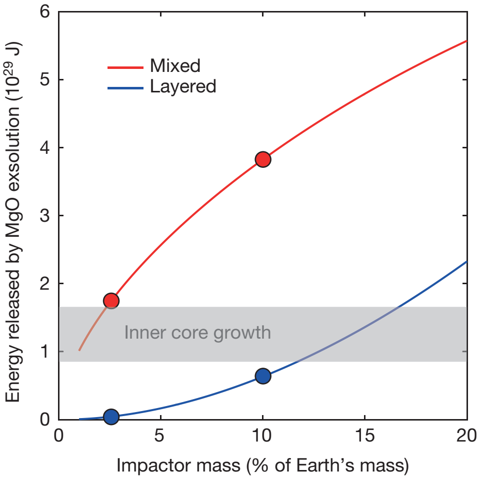

Figure 3 | Gravitational energy released by the exsolution of buoyant mantle components from the core after the giant impact. Calculated following equation (3), the red curve corresponds to the energy released if the HIC fully mixes with Earth's core. In that case, MgO exsolution occurs up to the current saturation limit (Fig. 1b). The blue curve corresponds to the energy released if the HIC forms a layer on top of Earth's core. In that case, the layer is so rich in lithophile elements (Fig. 2a) that the exsolution of all dissolved mantle components (MgO and SiO_2) takes place. The Mars-size impact[19] (10% of Earth's mass) and fast-spinning impact[20] (2.5% of Earth's mass) are highlighted by circles. The grey horizontal band corresponds to the energy released by inner-core growth (gravitational + latent heat) since its inception, and is the main driver for the geodynamo today. The energies released by MgO exsolution are of the order of, if not higher than, those released by inner-core growth, and demonstrate the effectiveness of the exsolution of mantle components to drive an early dynamo. The average power of exsolution can be estimated assuming an exsolution time (Extended Data Fig. 8) or a temperature evolution model of the core (Extended Data Fig. 5).

required to run a geodynamo by compositional buoyancy[22]) over the course of exsolution (Extended Data Fig. 5). With the onset of inner-core growth, the cooling and exsolution rates decrease and the power drops to about 1 TW (see Methods). In terms of timing, the onset of exsolution occurs once the (decreasing) MgO saturation value at the CMB reaches the concentration in the core (Extended Data Fig. 5). For our nominal model, this occurs around 1 Gyr after Earth's formation with a Mars-sized impact and increases to approximately 2.3 Gyr in the case of a small, 'fast-spinning' impact (see Methods).

Rapid initial cooling following a giant impact may have driven an early thermal dynamo. However, our experimental results show that MgO exsolution probably dominated the energy budget of Earth's core in the intermediate period between early, rapid cooling and the onset of inner-core growth. This result provides a tangible basis for an exsolution-driven dynamo[7], as well as a plausible mechanism for explaining the uninterrupted geological record of magnetism[1] in Earth's rocks and minerals dating to 3.5 Gyr ago or earlier. This mechanism should be relatively ineffective in smaller planets such as Mars or on Earth-sized planets that have not experienced a giant impact; but for super-Earths, where pressures and temperatures could remain super-solvus for extended periods, it represents a new method of driving potentially detectable present-day dynamos.

Online Content Methods, along with any additional Extended Data display items and Source Data, are available in the online version of the paper; references unique to these sections appear only in the online paper.

Received 5 January; accepted 16 May 2016.

1. Tarduno, J. A. *et al.* Geodynamo, solar wind, and magnetopause 3.4 to 3.45 billion years ago. *Science* **327,** 1238–1240 (2010).
2. Nimmo, F. in *Treatise on Geophysics* 2nd edn, Vol. 8 (ed. Olson, P.) 27–55 (Elsevier, 2015).
3. Lister, J. R. & Buffett, B. A. The strength and efficiency of thermal and compositional convection in the geodynamo. *Phys. Earth Planet. Inter.* **91,** 17–30 (1995).
4. Labrosse, S., Poirier, J. P. & LeMouel, J. L. On cooling of the Earth's core. *Phys. Earth Planet. Inter.* **99,** 1–17 (1997).
5. Gubbins, D., Alfe, D., Masters, G., Price, G. D. & Gillan, M. J. Can the Earth's dynamo run on heat alone? *Geophys. J. Int.* **155,** 609–622 (2003).
6. Labrosse, S. Thermal evolution of the core with a high thermal conductivity. *Phys. Earth Planet. Inter.* **247,** 36–55 (2015).
7. O'Rourke, J. G. & Stevenson, D. J. Powering Earth's dynamo with magnesium precipitation from the core. *Nature* **529,** 387–389 (2016).
8. Ringwood, A. E. Chemical evolution of terrestrial planets. *Geochim. Cosmochim. Acta* **30,** 41–104 (1966).
9. Rubie, D. C., Melosh, H. J., Reid, J. E., Liebske, C. & Righter, K. Mechanisms of metal-silicate equilibration in the terrestrial magma ocean. *Earth Planet. Sci. Lett.* **205,** 239–255 (2003).
10. Wood, B. J., Walter, M. J. & Wade, J. Accretion of the Earth and segregation of its core. *Nature* **441,** 825–833 (2006).
11. Badro, J., Brodholt, J. P., Piet, H., Siebert, J. & Ryerson, F. J. Core formation and core composition from coupled geochemical and geophysical constraints. *Proc. Natl Acad. Sci. USA* **112,** 12310–12314 (2015).
12. Hartmann, W. K. & Davis, D. R. Satellite-sized planetesimals and lunar origin. *Icarus* **24,** 504–515 (1975).
13. Labrosse, S., Hernlund, J. W. & Coltice, N. A crystallizing dense magma ocean at the base of the Earth's mantle. *Nature* **450,** 866–869 (2007).
14. Buffett, B. A., Garnero, E. J. & Jeanloz, R. Sediments at the top of Earth's core. *Science* **290,** 1338–1342 (2000).
15. Stevenson, D. Core exsolution: a likely consequence of giant impacts and a likely energy source for the geodynamo. *Eos Trans. AGU* **88** (Fall Meet. Suppl.), abstr. U21D-02 (American Geophysical Union, 2007).
16. Buffett, B. A. Earth's core and the geodynamo. *Science* **288,** 2007–2012 (2000).
17. Wahl, S. M. & Militzer, B. High-temperature miscibility of iron and rock during terrestrial planet formation. *Earth Planet. Sci. Lett.* **410,** 25–33 (2015).
18. Nimmo, F. in *Treatise on Geophysics* 2nd edn, Vol. 9 (ed. Stevenson, D. J.) 201–219 (Elsevier, 2015).
19. Canup, R. M. Forming a Moon with an Earth-like composition via a giant impact. *Science* **338,** 1052–1055 (2012).
20. Cuk, M. & Stewart, S. T. Making the Moon from a fast-spinning earth: a giant impact followed by resonant despinning. *Science* **338,** 1047–1052 (2012).
21. Deguen, R., Landeau, M. & Olson, P. Turbulent metal-silicate mixing, fragmentation, and equilibration in magma oceans. *Earth Planet. Sci. Lett.* **391,** 274–287 (2014).
22. Aubert, J., Labrosse, S. & Poitou, C. Modelling the palaeo-evolution of the geodynamo. *Geophys. J. Int.* **179,** 1414–1428 (2009).
23. Badro, J., Cote, A. S. & Brodholt, J. P. A seismologically consistent compositional model of Earth's core. *Proc. Natl Acad. Sci. USA* **111,** 7542–7545 (2014).

Supplementary Information is available in the online version of the paper.

Acknowledgements The research leading to these results has received funding from the European Research Council under the European Community's Seventh Framework Programme (FP7/2007-2013)/ERC grant agreement no. 207467. Parts of this work were supported by the UnivEarthS Labex programme at Sorbonne Paris Cité (ANR-10-LABX-0023 and ANR-11-IDEX-0005-02), IPGP multidisciplinary programme PARI, and by Paris–IdF region SESAME grant no. 12015908. J.S. acknowledges support from the French National Research Agency (ANR project VolTerre, grant no. ANR-14-CE33-0017-01). We thank J. Aubert, S. Stewart and P. Asimow for discussions. We thank R. Ryerson for comments on the manuscript.

Author Contributions J.B. designed the project, performed the experiments, implemented the thermodynamic and core-formation modelling, discussed the results and wrote the manuscript. J.S. performed the experiments, discussed the results and commented on the manuscript. F.N. implemented the core exsolution energy modelling, discussed the results and commented on the manuscript.

Author Information Reprints and permissions information is available at www.nature.com/reprints. The authors declare no competing financial interests. Readers are welcome to comment on the online version of the paper. Correspondence and requests for materials should be addressed to J.B. (badro@ipgp.fr).

Reviewer Information *Nature* thanks B. Buffett and Y. Fei for their contribution to the peer review of this work.

METHODS

Magnesium and aluminium solubility. The thermodynamic process of lithophile element incorporation in iron involves the solubility of mantle components in the metal phase (equation (1)), rather than redox exchange as in the case of siderophile element partitioning. The magnesium concentration in the metal ranges between 0.2 mol% and 1 mol% in our experiments. The equilibrium constant of the dissolution reaction given in equation (1) (reprinted here for convenience):

$$\mathrm{MgO}^{\mathrm{silicate}} \rightleftharpoons \mathrm{Mg}^{\mathrm{metal}} + \mathrm{O}^{\mathrm{metal}}$$

is

$$K_{\mathrm{Mg}} = \frac{X_{\mathrm{Mg}}^{2}}{X_{\mathrm{MgO}}} \quad (4)$$

(where X_{Mg} is the mole fraction of Mg in the metal and X_{MgO} the mole fraction of MgO in the silicate) and its logarithm is proportional to the change in Gibbs free energy of the reaction defined by equation (1):

$$\log(K_{\mathrm{Mg}}) = a + \frac{b}{T} + c\frac{P}{T} \quad (5)$$

where the parameters a, b and c correspond to the changes in entropy, enthalpy and volume in the reaction in equation (1), respectively. These parameters were fitted to the data using linear regression, and c was found to be statistically irrelevant (no pressure dependence), yielding equation (2) (reprinted here for convenience):

$$\log(K_{\mathrm{Mg}}) = 1.23(\ 0.7) - \frac{18,816(2,600)}{T}$$

Similarly, the aluminium concentration of in the metal ranges from 0 mol% (below the detection limit, explaining two fewer points for the Al plot in Extended Data Fig. 2) to 1.1 mol%. The equilibrium constant of the dissolution reaction

$$\mathrm{Al_2O_3}^{\mathrm{silicate}} \rightleftharpoons 2\mathrm{Al}^{\mathrm{metal}} + 3\mathrm{O}^{\mathrm{metal}} \quad (6)$$

is

$$K_{\mathrm{Al}} = \frac{X_{\mathrm{Al}}^{2.5}}{X_{\mathrm{AlO_{1.5}}}} \quad (7)$$

(where X_{Al} is the mole fractions of Al in the metal and $X_{\mathrm{AlO_{1.5}}}$ the mole fraction of $\mathrm{AlO_{1.5}}$ in the silicate) Its logarithm is proportional to the change in Gibbs free energy of the reaction in equation (6) and can be written in the same form as equation (5); fitting to the data using linear regression shows that c is once again statistically irrelevant, and we find

$$\log(K_{\mathrm{Al}}) = 4.1(1.4) - \frac{36,469(5,260)}{T} \quad (8)$$

where the numbers in parentheses are the standard errors of the parameters.

Saturation conditions at the core–mantle boundary. Equations (2), (4), (7) and (8) allow us to calculate the Mg and Al concentrations in molten iron as a function of temperature and silicate composition. An important case is that of the equilibrium value in the core at the core–mantle boundary (CMB). As shown above, MgO dissolution in iron has no pressure dependence. This means that MgO exsolves in the coldest part of the core, which is the CMB. The equilibrium value at the CMB is therefore the MgO saturation value; if the MgO concentration in the core is above saturation, then MgO will be exsolved until it reaches that value. Figure 1b shows the equilibrium value of MgO concentration in the core as a function of CMB temperature, for a core buffered by (that is, in local equilibrium with) a pyrolitic magma ocean (50 mol% MgO in the mantle).

Experimental and analytical. The silicate glasses were produced in an aerodynamic levitation laser furnace. The starting mixes were made by grinding and mixing from pure oxide ($\mathrm{SiO_2}$, MgO, $\mathrm{Fe_2O_3}$, $\mathrm{Al_2O_3}$) and carbonate ($\mathrm{CaCO_3}$) components, pressing them into pellets, and then fusing them at constant oxygen fugacity at 1,900–2,100 °C for 5 min in a laser furnace using a 120-W $\mathrm{CO_2}$ laser. The fused samples were quenched to glasses, and analysed for recrystallization, homogeneity and composition on a Zeiss Auriga field-emission scanning electron microscope (IPGP, Paris). The glass beads were thinned down to 20-μm-thick double-parallel thin sections and were processed using a femtosecond laser machining platform to cut disks of identical size for loading in the diamond-anvil cell. Spherical iron balls 1–3 μm in size were flattened between two such silicate disks, and constituted the layered starting sample. Pressure was measured from the frequency shift of the first-order Raman mode in diamond, measured on the anvil tips. Temperature was measured every second, simultaneously from both sides, by spectroradiometry. Electronic laser shutdown operates in about 2–4 μs, and temperature quench occurs in approximately 10 μs (owing to thermal diffusion in the sample) ensuring an ultrafast quench of the sample.

After decompression, a thin section (20 μm × 10 μm wide, 1–3-μm thick) was extracted from the centre of the laser-heated spot using a Zeiss Auriga crossbeam focused-ion-beam microscope (IPGP, Paris). The sample was imaged and then transferred to a TEM copper grid, and the metal and silicate phases were analysed using a Cameca SX-Five electron microprobe (CAMPARIS, Paris) with five large-area analysers. Metal and silicate phases of the run products are large enough (>5 μm) to perform reliable analyses with an electron probe micro-analyser (EPMA) on focused ion beam (FIB) thin sections.

Metal and silicate phases were analysed using Cameca SX100 and Cameca SX FIVE (CamParis, UPMC–IPGP) electron probe micro-analysers. X-ray intensities were reduced using the CITZAF correction routine. Operating conditions were 15-kV accelerating voltage, and 10–20-nA beam current and counting times of 10–20 s on peak and background for major elements and 20–40 s for trace elements (including Mg and Al in the metallic phases). Pure Fe metal was used as standard for metal. $\mathrm{Fe_2O_3}$, $\mathrm{SiO_2}$, MgO and $\mathrm{Al_2O_3}$ were used as standards to measure solubility of oxygen, silicon, magnesium and aluminium in metal. Diopside glass (Si), wollastonite (Ca), orthoclase (K), anorthite (Al), albite (Na), rutile (Ti) and pure oxides ($\mathrm{Fe_2O_3}$, MgO, $\mathrm{SiO_2}$, CaO and $\mathrm{Al_2O_3}$) were used as standards for the silicate. We verified that the geometry of the metal and silicate phases was identical from both sides of the FIB sections, so that the EPMA analyses only a single phase. The EPMA uses a beam size of 1–2 μm, which is large enough to integrate the small quench features of metal and silicate phases (<200 nm) and to determine their bulk compositions. When a few small metallic blobs were present in the silicate (500 nm to 2 μm in diameter), special care was taken to avoid them during analysis of the silicates.

Core formation modelling. The core of Earth formed in the first approximately 50 million years[24,25] of the Solar System, by an iterative addition of material to the proto-Earth. The accreting material, consisting of mixtures of iron-rich metals and silicates similar to those found in extra-terrestrial bodies (such as chondrite parent bodies, HEDs and angrites), impacted the growing planet. The heat generated by those impacts maintained the outermost portion of the planet in a molten state known as a magma ocean[26]. At temperatures below the solvus of iron and silicate, the two phases un-mix and the metal (twice denser) segregates towards the centre and forms the core. Along with the segregating metal, the siderophile elements are stripped to the core, among which are light elements such as Si and O. The depletion of siderophile elements from the mantle has been widely used to constrain the pressure–temperature–composition path of core formation, and has shown that the core formed in a deep magma ocean[27,28]. As the planet accretes, the magma ocean grows deeper; recent models[11] show that the concentrations of Ni, Co, Cr and V in the mantle satisfy terrestrial observables for a final magma ocean depth of between 1,000 km and 1,700 km, corresponding to final pressures of between 40 GPa and 75 GPa and final temperatures of between 3,000 K and 4,180 K, respectively.

We ran a series of traditional multistage core-formation models[11] where the planet was accreted to its present mass in increments of 0.1% of Earth's mass, without giant impacts. At each stage, the planet grows and the pressure and temperature of equilibration increase accordingly. The concentrations of Ni, Co, V, Cr, O, Si and Mg in the core were calculated iteratively during the 1,000 steps of the accretion process. The simulations were run for a variety of redox paths (ranging from very reduced to very oxidized), several geotherms (between the solidus and the liquidus of peridotite), and for all possible magma ocean depths, ranging from 0% (magma lake) to 100% (fully molten Earth) of the mantle. We forward-propagated all uncertainties on the thermodynamic parameters governing the partitioning equations using Monte Carlo simulation. Most models (very deep or very shallow) do not satisfy, within uncertainties, the observed geochemical abundances of Ni, Co, V and Cr in the mantle and therefore are not relevant. We selected only the models that do reproduce the geochemical abundances of Ni, Co, V and Cr in the present-day mantle, and found that the maximum MgO concentration in the core at the end of accretion is 0.8 wt%.

Giant-impact modelling. In the Moon-forming giant-impact scenario[12], the impactor is typically thought of as a Mars-sized planetary embryo, but the masses used in models range from 2.5% to 20% of Earth's mass[19,20]. With such a size, the impactor is a differentiated object with a core and mantle (as opposed to small undifferentiated bodies) and, hence, it does not fully equilibrate with the entire magma ocean, but rather partially equilibrates[29] with a small portion[9,21] of that magma ocean. The impactor and the magma ocean (in the impact zone) reach tremendous temperatures during the impact, as shown by smoothed-particle hydrodynamic simulations[19,20]. Even though the temperatures from those simulations can be inaccurate because of intrinsic inaccuracies in the equations of state that they are based on, the minimum temperature[19] for the impactor core is

8,000 K and that of the magma ocean in the impacted area is 7,000 K. Therefore, the system consisting of the impactor core and the surrounding silicate mantle is necessarily always hotter than 7,000 K, and turns into a single miscible metal-silicate phase.

We calculated the composition of Earth's core after the giant impact in two steps. First, we modelled the pre-giant-impact accretionary phase. The Earth was partially accreted, as described in the previous paragraph, until it reached 80% to 99% of Earth's mass, leaving the planet in the state it was in before the giant impact. We considered only the models that reproduce the present-day geochemical abundances of Ni, Co, V and Cr in the mantle. Then the final accretion event took place, consisting of the giant impact bringing in the remaining 1% to 20% of Earth's mass. We calculated the composition of the hybridized impactor core (HIC) as a function of its size (Fig. 2a) by considering the fact that, as opposed to small accretionary building blocks, the core of the giant impactor does not fully equilibrate with the entire magma ocean; instead, it partially equilibrates[29] with a small portion[9,21] of the magma ocean (see Methods section 'Partial core equilibration and turbulent fragmentation and mixing' below). It is clear from Fig. 2a that the bigger the impactor, the smaller the relative mass of magma ocean it interacts and equilibrates with and, consequently, the less mantle components (Mg, O, Si) the HIC contains. The net effect on Earth's core, once the HIC is added, is mitigated as shown in Fig. 2b; it is the result of the balance between larger HICs being less enriched in mantle component, but contributing more mass to the whole core.

Partial core equilibration and turbulent fragmentation and mixing. The composition of the HIC was calculated by taking into account two main parameters that are usually neglected in traditional core-formation models[9–11,28,30].

First, the degree of partial equilibration—that is, the fraction of the core that equilibrates with the mantle—has been constrained by geochemical modelling, from the combined analysis of the Hf–W and U–Pb isotopic systems, and shown to be at least[25,29,31] 40%. We used this conservative lower bound, meaning that 60% of the impactor core merges with Earth's core without equilibration (and therefore with no compositional effect), whereas the other half equilibrates in the magma ocean before merging with the core.

Second, the impactor core only 'sees' a portion[9] of the magma ocean, with the fraction involved in the equilibration estimated from fragmentation and turbulent mixing scaling laws[21]; these laws show that the ratio of equilibrated silicate to equilibrated metal (dilution ratio Δ) in the magma ocean is given by

$$\Delta = \frac{\rho_{\text{silicate}}}{\rho_{\text{metal}}}\left[\left(1+\frac{0.25}{\delta^{1/3}}\right)^{3} - 1\right]$$

where ρ_{silicate} and ρ_{metal} are the densities of silicate and metal, and δ is the ratio of impactor to Earth mass.

MgO exsolution energy. The energy release depends on how the HIC mixes with Earth's core, as shown by the dependence on $\rho(r)$ in equation (3). Even though simulations[20] and energetic arguments[32] suggest that the HIC should thoroughly mix with Earth's core, we investigated two extreme models of mixing: (i) full mixing of the HIC with Earth's core producing a homogeneous core and (ii) full layering where the HIC sits atop Earth's core.

In the mixed case, the HIC is diluted in the bulk of Earth's core and therefore the Si and O content delivered by the impactor are below the saturation limit of those elements[11,30,33] (Fig. 2b); those concentrations are under-saturated with respect to the overlying conditions imposed by the magma ocean at the CMB, and there is no chemical drive to force those components out of the system. In that case, we considered that MgO is the only phase to exsolve so that the associated energy release is a conservative lower bound.

In the layered case, the HIC is concentrated atop the proto-core, and all three mantle components (MgO, SiO_2 and FeO) are highly concentrated in the layer and over-saturated with respect to CMB conditions prevailing atop that layer. In that case, all of those components would exsolve and remix with the overlying magma ocean.

In our energy calculations, we fixed the present-day CMB temperature to 4,100 K. Lower temperatures imply a lower saturation level in the core, and mean that more MgO exsolves and more energy is produced, and vice versa. The final density and radius of the core are the present-day values (10.6 g cm^{-3} and 3,485 km, respectively).

Impactor core mixing. We considered a uniform core of density ρ and radius R; it subsequently undergoes un-mixing into an inner (dense) region with density ρ_c and radius R_c (the present-day values given above), and an outer buoyant layer with density ρ_{layer}. The volume fraction of the outer layer is f, which we take to be $\ll 1$. We may write

$$\rho = (1-f)\rho_c + f\rho_{layer} \tag{9}$$

and

$$R_c = (1-f/3)R \tag{10}$$

where equation (10) is correct to first order in f. In practice, we specify ρ_c and ρ_{layer} (4.8 g cm^{-3} for MgO) and calculate ρ and R for a given value of f, with the current core boundary taken to be R_c. The gravitational energy E of the core in either state may be derived using equation (3), and the change in energy ΔE in going from the uniform to the unmixed state can be available to do work (for example, to drive a dynamo). Making use of equations (3), (9) and (10), it may be shown that, to first order in f:

$$\Delta E = \frac{16}{45}\pi^2 G R^5 f\rho_c(\rho_c - \rho_{\text{layer}}) \tag{11}$$

For $f = 20\%$, equation (11) overestimates the full calculation (plotted in the figures) by about 5%; the discrepancy is smaller with smaller f, and equation (11) can be used, to a good approximation, to estimate the amount of energy released by mantle-component exsolution from the core. This equation shows the correct limiting behaviour in the cases of $f = 0$ and $\rho_c = \rho_{\text{layer}}$.

Impactor core layering. In this case we take the mass fraction of the Earth's core added by the HIC to be f_m. With a HIC density of ρ_i and a present-day total core mass of M_c, the radius of the base of the impactor layer R_1 before un-mixing of this layer is given by

$$R_1^3 = R^3 - \frac{3 f_m M_c}{4\pi\rho_i}$$

The HIC layer then undergoes un-mixing into two components: 'mantle components' (ρ_2, 5.6 g cm^{-3}) and 'core material' (ρ_1, 10.6 g cm^{-3}). The HIC density ρ_i may then be derived using

$$(R^3 - R_1^3)\rho_i = (R_2^3 - R_1^3)\rho_1 + (R^3 - R_2^3)\rho_2$$

where R_2 is the radius of the base of the light-element layer after un-mixing. To make the total core mass correct, the density of the pre-impact core, ρ_c, is also calculated. Once ρ_i, R_1 and R_2 have been calculated, the energy change due to un-mixing within the layer can be calculated using successive applications of equation (11), as before.

Thermal evolution and exsolution power. Using a CMB temperature evolution model, we can estimate the MgO exsolution rate and, hence, an exsolution power, as a function of time. A typical CMB temperature evolution is shown in Extended Data Fig. 4a, along with the associated MgO content of the core (Extended Data Fig. 4b) obtained by rewriting the MgO equilibrium curve (Fig. 1b) as a function of time. The time derivatives are the cooling rate of the core and its MgO exsolution rate as a function of time, and are plotted in Extended Data Fig. 4c, d, respectively.

Very early in Earth's history, the core was so hot that the equilibrium MgO concentration at the CMB (Extended Data Fig. 4b) is higher than the MgO content of the core, and no exsolution occurs. The reverse reaction—that is, the potential for MgO to be dissolved from the mantle to the core—is limited; it is prone to affect only a thin layer below the CMB that is enriched in MgO, that becomes light and stably stratified, and that is therefore unable to recycle and affect the entire core. As the core cools, exsolution starts once the temperature at the CMB reaches a critical value corresponding to an MgO equilibrium concentration equal to that in the core. This is shown in Extended Data Fig. 5, and is highlighted for two models: the Mars-size impact[19] leaving behind a core containing 2.9 wt% MgO and a small fast-spinning impact[20] producing a core containing 2.1 wt% MgO (see Fig. 2b and Extended Data Fig. 3). The power produced by MgO exsolution is linked to the exsolution rate, and can be estimated from the energy release (Fig. 3 and Extended Data Fig. 8) to be between 5.5 TW wt% Gyr^{-1} and 7 TW wt% Gyr^{-1}. This estimate allows us to translate an exsolution rate (Extended Data Fig. 4d) into exsolution power, as shown in Extended Data Figs 5b and 8.

What is noteworthy is that the initial MgO core content does not directly affect exsolution power. The latter is a function of only the exsolution rate, which is itself a function of core cooling rate. Initial MgO content sets only the onset of exsolution, as shown in Extended Data Fig. 5. Of course, higher MgO contents in the core entail an earlier onset of exsolution, a longer duration for buoyancy-driven exsolution power and, hence, much higher total exsolution energies, as shown in Fig. 3. This dichotomy could be mitigated had we self-consistently included MgO exsolution in the thermal evolution model of the core. MgO exsolution power markedly drops with the onset of inner-core growth, as a consequence of the drop in core cooling rate. At the present day, MgO exsolution should still produce about 1 TW of power, much lower than the approximately 3 TW produced by inner-core growth and driving the geodynamo. However, before inner-core growth, exsolution power is always higher than about 3 TW, demonstrating that MgO exsolution can conceivably drive a geodynamo as early as around 1 Gyr after core formation, and until the onset of inner-core growth.

The geodynamo. Assuming an entirely bottom-driven present-day dynamo, corresponding to a CMB heat flow exactly at the adiabatic value (Q_{ad}) of 15 TW (refs 34,35), the convective power sustaining the geomagnetic field $P = \varepsilon Q_{ad}$ is 3 TW, where $\varepsilon = 0.2$ is the thermodynamic efficiency of latent heat and light-element release at the inner-core boundary[22]. Power-based scaling laws of the magnetic intensity[36] then predict an internal magnetic field of about 1–4 mT, the higher estimate being in agreement with the observation of magnetic Alfvén waves in the core[37] coupled to length-of-day variations at periods close to 6 years (ref. 38).

Dynamo strength increases as buoyancy flux increases[39,40], so the MgO exsolution mechanism represents a potent driver of an early geodynamo[7]. Although a giant impact might cause thermal stratification in the core[6,41], the stabilizing thermal buoyancy will be completely overwhelmed by the compositional buoyancy associated with MgO exsolution.

24. Kleine, T., Mezger, K., Munker, C., Palme, H. & Bischoff, A. Hf-182-W-182 isotope systematics of chondrites, eucrites, and martian meteorites: chronology of core formation and early mantle differentiation in Vesta and Mars. *Geochim. Cosmochim. Acta* **68,** 2935–2946 (2004).
25. Yin, Q. Z. *et al.* A short timescale for terrestrial planet formation from Hf-W chronometry of meteorites. *Nature* **418,** 949–952 (2002).
26. Murthy, V. R. Early differentiation of the Earth and the problem of mantle siderophile elements: a new approach. *Science* **253,** 303–306 (1991).
27. Li, J. & Agee, C. B. Geochemistry of mantle–core differentiation at high pressure. *Nature* **381,** 686–689 (1996).
28. Siebert, J., Badro, J., Antonangeli, D. & Ryerson, F. J. Metal-silicate partitioning of Ni and Co in a deep magma ocean. *Earth Planet. Sci. Lett.* **321–322,** 189–197 (2012).
29. Rudge, J. F., Kleine, T. & Bourdon, B. Broad bounds on Earth's accretion and core formation constrained by geochemical models. *Nat. Geosci.* **3,** 439–443 (2010).
30. Siebert, J., Badro, J., Antonangeli, D. & Ryerson, F. J. Terrestrial accretion under oxidizing conditions. *Science* **339,** 1194–1197 (2013).
31. Kleine, T., Mezger, K., Palme, H. & Munker, C. The W isotope evolution of the bulk silicate Earth: constraints on the timing and mechanisms of core formation and accretion. *Earth Planet. Sci. Lett.* **228,** 109–123 (2004).
32. Nakajima, M. & Stevenson, D. J. Dynamical mixing of planetary cores by giant impacts. *Lunar Planet. Sci. Conf.* **47,** 2053, http://www.hou.usra.edu/meetings/lpsc2016/pdf/2053.pdf (2016).
33. Fischer, R. A. *et al.* High pressure metal-silicate partitioning of Ni, Co, V, Cr, Si, and O. *Geochim. Cosmochim. Acta* **167,** 177–194 (2015).
34. Pozzo, M., Davies, C., Gubbins, D. & Alfè, D. Thermal and electrical conductivity of iron at Earth's core conditions. *Nature* **485,** 355–358 (2012).
35. de Koker, N., Steinle-Neumann, G. & Vlcek, V. Electrical resistivity and thermal conductivity of liquid Fe alloys at high P and T, and heat flux in Earth's core. *Proc. Natl Acad. Sci. USA* **109,** 4070–4073 (2012).
36. Christensen, U. R. A deep dynamo generating Mercury's magnetic field. *Nature* **444,** 1056–1058 (2006).
37. Gillet, N., Jault, D., Canet, E. & Fournier, A. Fast torsional waves and strong magnetic field within the Earth's core. *Nature* **465,** 74–77 (2010).
38. Buffett, B. A. Gravitational oscillations in the length of day. *Geophys. Res. Lett.* **23,** 2279–2282 (1996).
39. Olson, P. & Christensen, U. R. Dipole moment scaling for convection-driven planetary dynamos. *Earth Planet. Sci. Lett.* **250,** 561–571 (2006).
40. Christensen, U. R. & Aubert, J. Scaling properties of convection-driven dynamos in rotating spherical shells and application to planetary magnetic fields. *Geophys. J. Int.* **166,** 97–114 (2006).
41. Arkani-Hamed, J. & Olson, P. Giant impacts, core stratification, and failure of the Martian dynamo. *J. Geophys. Res. Solid Earth* **115,** E07012 (2010).

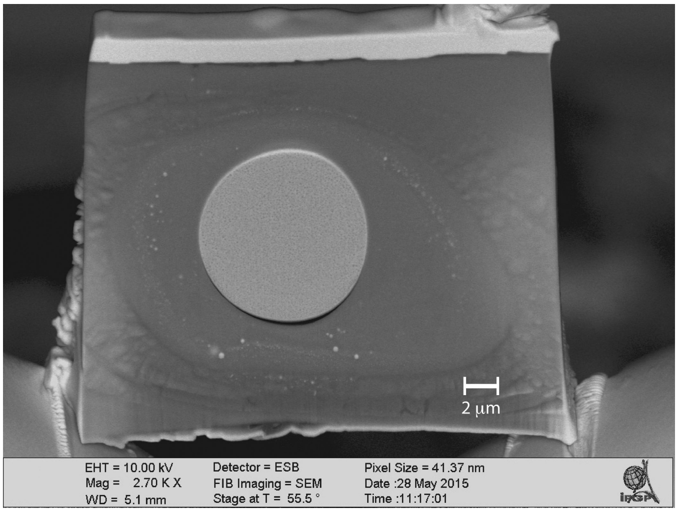

Extended Data Figure 1 | A fully molten metal-silicate sample recovered from the laser-heated diamond-anvil cell. A backscattered electron scanning electron microscopy image of a thin section recovered from a laser-heated diamond-anvil cell experiment. The section is excavated and lifted out from the centre of the heated region, then thinned down to 3 μm using a focused-ion-beam instrument. The metal and the silicate are both fully molten, as indicated by the coalesced metallic ball in the centre and the circular rim of silicate around it. This sample was compressed to 55 GPa and heated to 3,600 K for 60 s.

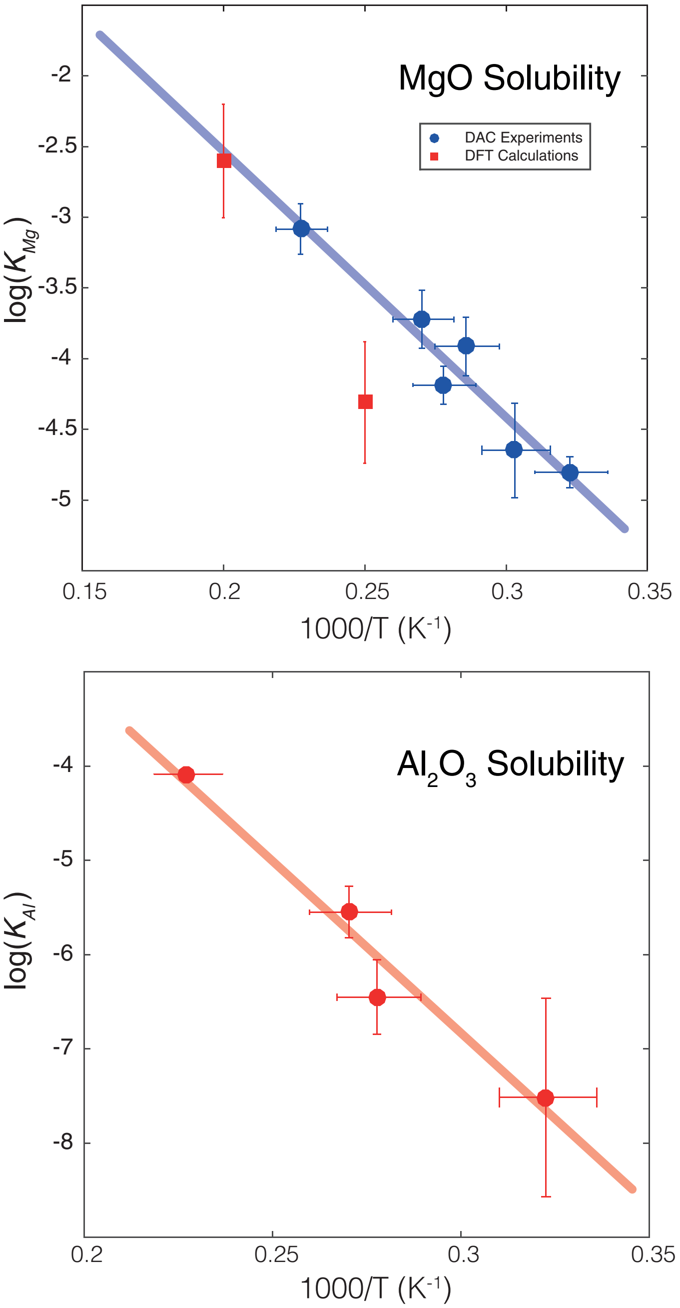

Extended Data Figure 2 | Magnesium and aluminium solubility in metallic iron melt at high pressure and temperature. Top, Equilibrium constant for MgO dissolution in molten iron (K_{Mg}) as a function of reciprocal temperature (1,000/T). The blue circles correspond to the experimental data (performed in a diamond-anvil cell, DAC; Extended Data Table 1) and the error bars to standard error; the red squares correspond to the low-temperature extrapolation of DFT calculations[17] and the error bars to standard error. The thick line corresponds to the least-squares linear fit to the experimental data (Fig. 1); it shows the agreement between the theoretical and experimental datasets, especially at high temperature where the theoretical dataset (which is extrapolated from higher temperatures) is the least influenced by extrapolation. Bottom, Equilibrium constant for Al_2O_3 dissolution (K_{Al}; see Methods) in molten iron as a function of reciprocal temperature. The circles correspond to the experimental data (Extended Data Table 1) and the error bars to standard error. The thick line corresponds to the least-squares linear fit to the data ($R^2 = 0.92$), and we find $\log(K_{\mathrm{Al}}) = 4.1(1.4) - 36{,}469(5{,}260)/T$ (equation (8)).

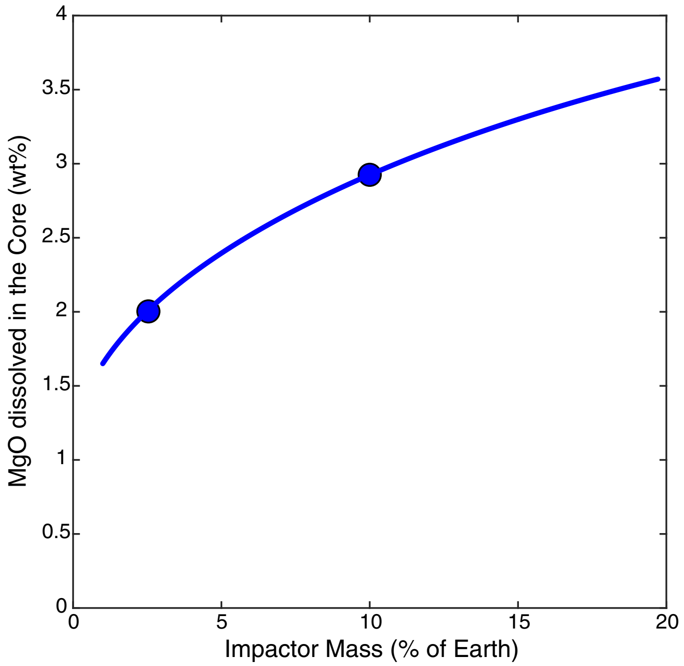

Extended Data Figure 3 | Total MgO dissolved in the core after the giant impact. A companion to Fig. 2, showing the sum of the MgO component dissolved in the core before the impact (0.8 wt%) and that brought by the HIC. The Mars-size impact[19] (10% of Earth's mass) and the fast-spinning impact[20] (2.5% of Earth's mass) are highlighted by circles, and provide 2.9 wt% and 2 wt% MgO to the core, respectively.

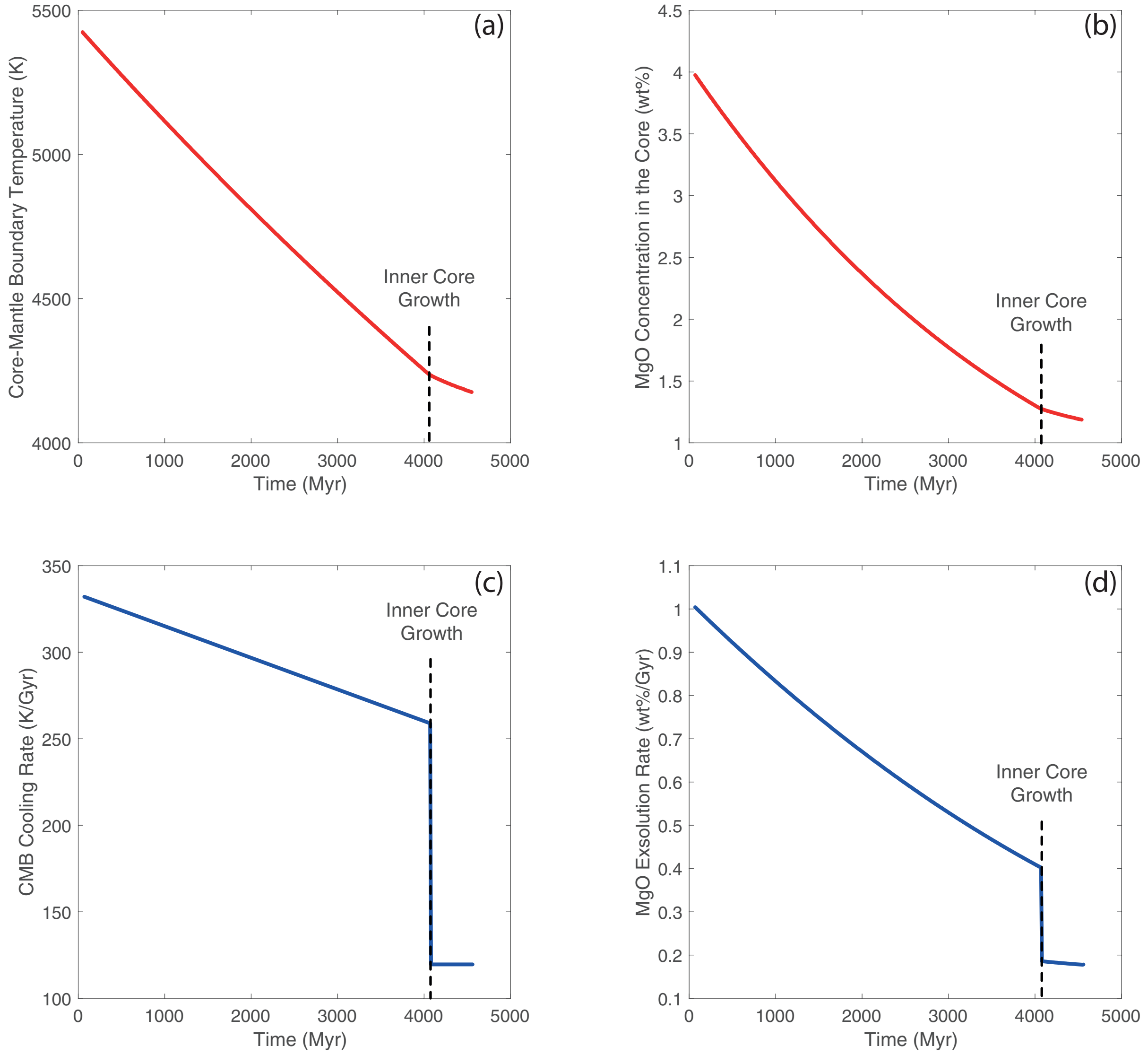

Extended Data Figure 4 | Thermal evolution of the core and MgO exsolution rate. a, **c**, Example CMB temperature evolution as a function of time (after Earth formation; Ga, billions of years ago), calculated using the same input parameters as in figure 4a of ref. 18 (**a**) and its derivative (**c**), which is the cooling rate. **b**, **d**, The associated MgO equilibrium concentration in the core (**b**), obtained by turning the temperature dependence in Fig. 1b into time dependence and its derivative (**d**), which is the exsolution rate. MgO will start exsolving from the core only when the MgO equilibrium concentration (**b**) drops below the MgO content in the core inherited from core formation and the giant impact. The core cooling rate and therefore the MgO exsolution rate drop markedly with the onset of inner-core growth. The core at the present day is still exsolving MgO, albeit at a much slower rate than that before inner-core growth.

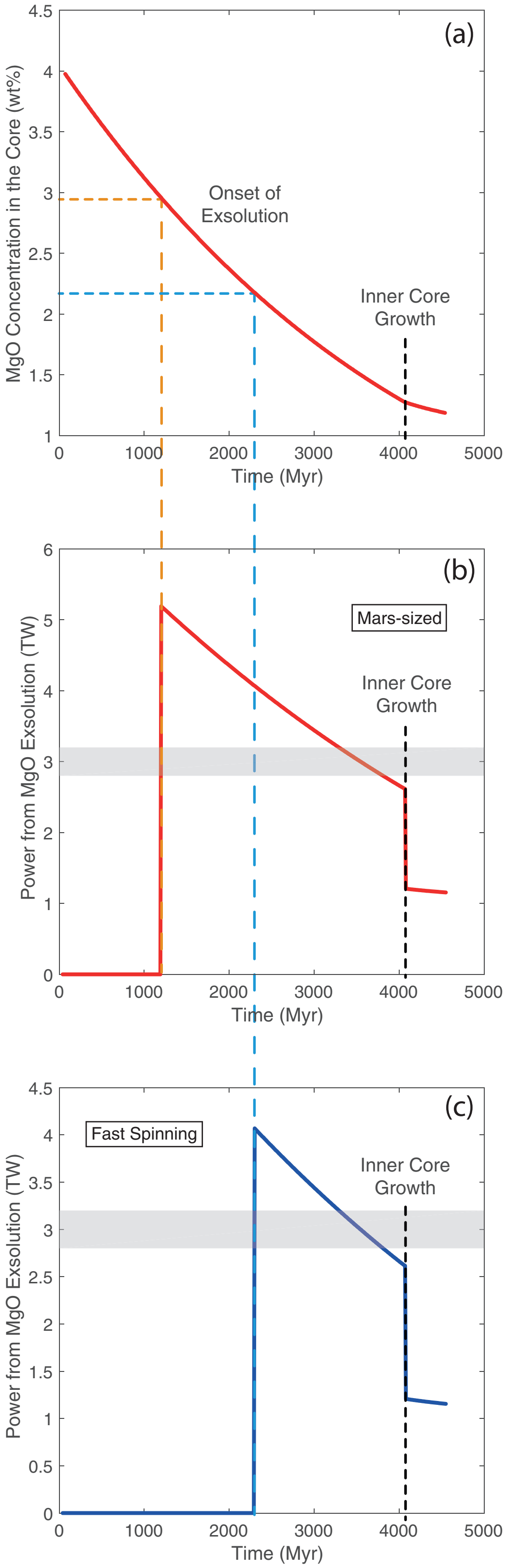

Extended Data Figure 5 | Onset of MgO exsolution and associated exsolution power for two typical models. a, The MgO equilibrium concentration in the core (same figure as Extended Data Fig. 4b), corresponding to our nominal CMB temperature evolution. The onset of MgO exsolution from the core occurs when the MgO equilibrium concentration drops below the MgO content in the core, which is reported here in two cases: 2.9 wt% for the Mars-sized impactor and 2.1 wt% for the fast-spinning impactor. For the thermal evolution model in Extended Data Fig. 4a, this onset is at 1.1 Gyr ago and 2.3 Gyr ago, respectively. **b**, **c**, Exsolution power for these two cases, which is proportional to the MgO exsolution rate plotted in Extended Data Fig. 4d. The power at a given time is independent of initial MgO content (as long as MgO is being exsolved). The initial MgO content affects only the onset of exsolution and therefore the duration of energy release. The power produced is in excess of 3 TW and is therefore sufficient to drive a dynamo by compositional buoyancy. The power drops markedly with the onset of inner-core growth, owing to the associated drop in the core cooling rate and the MgO exsolution rate. The core at the present day is still exsolving MgO and should produce about 1 TW of power, less than the power produced by inner-core growth.

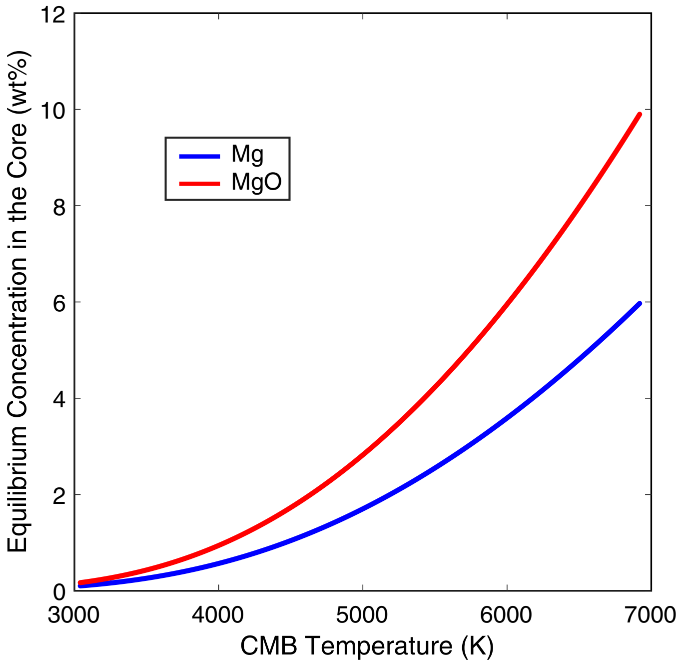

Extended Data Figure 6 | Equilibrium Mg and MgO concentration in the core as a function of CMB temperature. This is obtained by rewriting $\log(K_{\mathrm{Mg}}) = 1.23 - 18{,}816/T = 2\log(X_{\mathrm{Mg}}) - \log(X_{\mathrm{MgO}})$ as $\log(X_{\mathrm{Mg}}) = [1.23 - 18{,}816/T + \log(X_{\mathrm{MgO}})]/2$ with $X_{\mathrm{MgO}} = 0.5$ (pyrolitic mantle). This curve (red for MgO, blue for Mg) allows us to determine the magnesium saturation in the core at a given temperature. This threshold is important to estimate: (i) the present-day MgO content of the core and, hence, the amount of MgO lost by exsolution over geologic time (Extended Data Fig. 4) and (ii) the temperature at which MgO exsolution started after core formation (Extended Data Fig. 5). For instance, for a core containing 2.9 wt% MgO (for a Mars-sized impact; see Extended Data Fig. 3), exsolution is not bound to occur until the temperature at the CMB cools below 5,030 K. Moreover, if the present-day CMB temperature is 4,100 K, then the MgO saturation in the present-day core is 1.1 wt%, so that the total amount of MgO that can be exsolved from the core is not the total initial MgO content, but that amount minus the present-day saturation value.

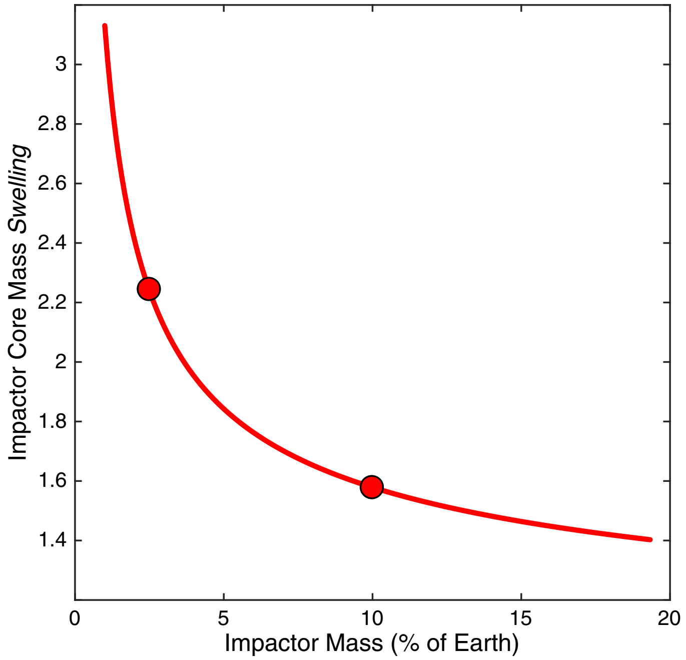

Extended Data Figure 7 | Chemical effect of equilibration of the impactor's core in Earth's magma ocean. Another companion to Fig. 2, showing the 'swelling' of the impactor core to form the hybridized impactor core (HIC). The HIC is larger than the impactor core because of the dissolved mantle components therein, which can represent up to two times its initial mass. This *y* axis shows the swelling factor, that is, the ratio of the mass of the HIC to that of the impactor core ($M_{\mathrm{HIC}}/M_{\mathrm{IC}}$). This swelling factor is equivalent to an effective dilution ratio. Small impactors interact with larger relative fractions of the magma ocean; therefore, they incorporate more mantle components per unit mass than do large impactors and so swell more. The HIC of a fast-spinning impactor[20] (2.5% of Earth's mass) is 2.2 times larger than the original impactor core, with 45% of its mass made up of initial impactor core material (iron) and the remaining 55% consisting of magma ocean components, as shown in Fig. 2a. The core of a Mars-sized impactor[19] (10% of Earth's mass) is 60% larger after equilibration with the magma ocean.

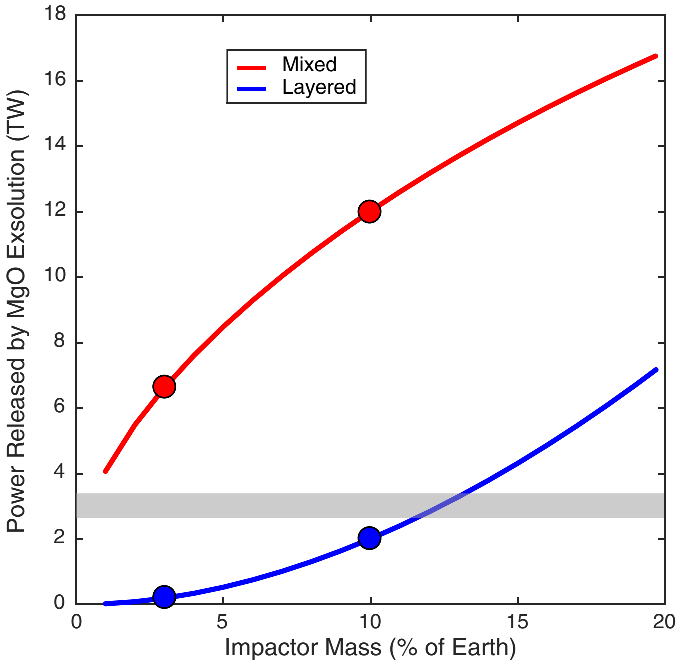

Extended Data Figure 8 | Power released by exsolution if it occurs over 1 Gyr. A companion to Fig. 3, showing how the gravitational energy released by exsolution is converted into average power, assuming a characteristic time of exsolution of 1 Gyr. The red curve corresponds to the energy released if the HIC fully mixes with Earth's core and the blue curve corresponds to the energy released if the HIC forms a layer on top of Earth's core. The grey horizontal band corresponds to 3 TW—the power driving the dynamo today—and thus provides a conservative estimate as to how much power is required to run a geodynamo by compositional buoyancy[22]. The Mars-size impact[19] (10% of Earth's mass) and fast-spinning impact[20] (2.5% of Earth's mass) are highlighted by circles. The blue curve represents a lower bound on the energy released in the case of layering of the HIC, because the layer contains so many mantle components that they would exsolve much faster, producing more power, albeit during a shorter period. By proportionality, this plot can be used to infer the power release for any characteristic exsolution time.

Extended Data Table 1 | Analyses of the Mg and Al concentrations in the metal and silicate phases of the experimental runs

Run	X1_2	X1_3	X1_4	X2_4	X4_2	X6_1
P (GPa)	71 (5)	35 (3)	50 (4)	74 (5)	55 (4)	43 (3)
T (K)	3500 (140)	3300 (130)	3700 (150)	4400 (180)	3600 (150)	3100 (130)
Mg (metal)	0.0042	0.0017	0.0088	0.0094	0.0053	0.0026
std err	0.0006	0.0004	0.0012	0.0011	0.0005	0.0002
MgO (silicate)	0.1446	0.1285	0.4081	0.1073	0.4324	0.4285
std err	0.0062	0.0034	0.0286	0.0072	0.0036	0.0070
log K_D	-3.9	-4.7	-3.7	-3.1	-4.2	-4.8
std err	0.19	0.35	0.21	0.18	0.13	0.10
Al (metal)			0.0018	0.0113	0.0008	0.0003
std err			0.0003	0.0002	0.0002	0.0002
$AlO_{1.5}$ (silicate)			0.0486	0.1651	0.0512	0.0511
std err			0.0036	0.0068	0.0012	0.0013
log K_D			-5.5	-4.1	-6.5	-7.4
std err			0.26	0.05	0.39	1.07

Experimental conditions (pressure in gigapascals, temperature in kelvin, uncertainties (standard error) in parentheses) and phase composition; all compositions are in molar fractions and standard errors are 1σ. The values for $\log(K_{Mg})$ and $\log(K_{Al})$ are plotted in Fig. 1 and Extended Data Fig. 2. Full chemical analyses of the samples are provided as Supplementary Data.